

## First principles phase diagram calculation for the 2D TMD system $WS_2-WTe_2$

Burton, B. P.; Sluiter, M. H.F.

**DOI**

[10.1016/j.calphad.2018.08.001](https://doi.org/10.1016/j.calphad.2018.08.001)

**Publication date**

2018

**Document Version**

Accepted author manuscript

**Published in**

Calphad: Computer Coupling of Phase Diagrams and Thermochemistry

**Citation (APA)**

Burton, B. P., & Sluiter, M. H. F. (2018). First principles phase diagram calculation for the 2D TMD system  $WS_2-WTe_2$ . *Calphad: Computer Coupling of Phase Diagrams and Thermochemistry*, 63, 142-147. <https://doi.org/10.1016/j.calphad.2018.08.001>

**Important note**

To cite this publication, please use the final published version (if applicable). Please check the document version above.

**Copyright**

Other than for strictly personal use, it is not permitted to download, forward or distribute the text or part of it, without the consent of the author(s) and/or copyright holder(s), unless the work is under an open content license such as Creative Commons.

**Takedown policy**

Please contact us and provide details if you believe this document breaches copyrights. We will remove access to the work immediately and investigate your claim.

# First Principles Phase Diagram Calculation for the 2D TMD system $WS_2 - WTe_2$ .

B. P. Burton<sup>a</sup>, M.H.F. Sluiter<sup>b</sup>

<sup>a</sup>Materials Measurement Laboratory, National Institute of Standards and Technology (NIST), Gaithersburg, MD 20899, USA;  
benjamin.burton@nist.gov

<sup>b</sup>Dept. MSE/3ME, Delft University of Technology, Mekelweg 2, 2628 CD Delft, The Netherlands; m.h.f.sluiter@tudelft.nl

---

## Abstract

First principles phase diagram calculations, that included van der Waals interactions, were performed for the bulk transition metal dichalcogenide system  $(1 - X) \cdot WS_2 - (X) \cdot WTe_2$ . To obtain a converged phase diagram, a series of cluster expansion calculations were performed with increasing numbers of structural energies, ( $N_{str}$ ) up to  $N_{str} = 435$ , used to fit the cluster expansion Hamiltonian. All calculated formation energies are positive and all ground-state analyses predict that formation energies for supercells with 16 or fewer anion sites are positive; but when  $150 \lesssim N_{str} \lesssim 376$ , false ordered ground-states are predicted. With  $N_{str} \geq 399$ , only a miscibility gap is predicted, but one with dramatic asymmetry opposite to what one expects from size-effect considerations; i.e. the calculations predict more solubility on the small-ion S-rich side of the diagram and less on the large-ion Te-rich side. This occurs because S-rich low-energy metastable ordered configurations have lower energies than their Te-rich counterparts which suggests that elastic relaxation effects are not dominant for the shape of the miscibility gap.

**Keywords:**  $WS_2 - WTe_2$ ; First Principles; Phase diagram calculation; van der Waals; transition metal dichalcogenide, TMD.

---

## 1. Introduction

There is great interest in two-dimensional (2D) transition metal dichalcogenide (TMD) materials  $MX_2$ , where M = Mo, W, Nb, Re, etc. and X = S, Se, or Te. [1, 2]. Currently, interest is focused on applications such as: band-gap engineering [3, 4]; nano-electronic devices [2, 5, 6, 7]; photovoltaic devices [8, 9]; valleytronics applications [10, 11]; 2D building blocks for electronic heterostructures [12]; and as sensors [13].

The bulk 2H crystal structure ( $P6_3/mmc$  space group) has AB-stacking of three-atom-thick 2D-layers that are bonded by van der Waals forces. Hence van der Waals forces influence bulk and multilayer phase relations and therefore anion order-disorder and/or phase separation in TMD solid solutions. The results presented below, for bulk  $WS_2 - WTe_2$ , imply that van der Waals interactions may strongly affect phase stabilities, either between adjacent layers in bulk or few-layer samples, or between monolayers and substrates.

Previous work on bulk  $(1 - X) \cdot MoS_2 - (X) \cdot MoTe_2$  [14] predicted two entropy stabilized incommensurate phases at  $X \approx 0.46$ , and this work was done to see if a similar prediction applies to the structurally analogous  $(1 - X) \cdot WS_2 - (X) \cdot WTe_2$  system. In the  $WS_2 - WTe_2$  system, however, only a miscibility gap is predicted, but a very large number of formation energy calculations,  $N_{str} \lesssim 400$ , is required to suppress false ground-states (GS). Also, the asymmetry of the calculated phase diagram is the opposite of what one expects from a size-effect argument [15, 16]; typically there is more solubility of the smaller ion in larger-ion-rich solutions (more S-solubility in Te-rich solutions) than vice versa;  $R_S = 1.84 \text{ \AA}$ ;  $R_{Te} = 2.21 \text{ \AA}$ . [17] In  $WS_2 - WTe_2$ , phase diagram asymmetry reflects the energy landscape for low-energy metastable states. Miscibility gaps in band-structure engineering materials, such as TMD alloys, are of particular concern to experimentalists because they imply the difficulty (impossibility) of synthesizing homogeneous alloys with continuously varying band-gaps.

## 2. Methodology

### 2.1. Total Energy Calculations

Total structural energies were calculated for fully relaxed  $WS_2$ ,  $WTe_2$  and for 433  $W_{m+n}(S_mTe_n)_2$  supercells. The Vienna *ab initio* simulation program (VASP, version 5.3.3 [18, 19]) was used for all density-functional theory (DFT) calculations, with projector augmented waves (PAW) and a generalized gradient approximation (GGA) for exchange energies. Electronic degrees of freedom were optimized with a conjugate gradient algorithm. Valence electron configurations were: W  $4d^5 5s^1$ ; S  $3s^2 3p^4$ ; Te  $5s^2 5p^4$ . Van der Waals interactions were modeled with the non-local correlation functional of Klimes *et al.* [20]. A 500 eV cutoff-energy was used in the “high precision” option, which converges *absolute* energies to within a few meV/chalogen atom (a few tenths of a kJ/mol of exchangeable S- and Te-anions). Precision is at least an order of magnitude better. Residual forces of order 0.02 eV or less were typical. VASP files describing the 433 total energy calculations are posted in the First Principles Phase Stability Repository. [21]

### 2.2. The Cluster Expansion Hamiltonian

Cluster expansion Hamiltonians (CEH) [22], were fit to sets of 71, 253, 295, 399, and 435 total energies (zero pressure formation enthalpies),

$$\Delta E_f[W_{m+n}(S_mTe_n)_2] = \frac{E[W_{m+n}(S_mTe_n)_2] - mE[WS_2] - nE[WTe_2]}{2(m+n)}, \quad (1)$$

where:  $E[W_{m+n}(S_mTe_n)_2]$  is the energy of the  $W_{m+n}(S_mTe_n)_2$  supercell.  $\Delta E_f$  as computed from the *ab initio* energies, is displayed as solid dots (green online) in Figs. 1a-5a. Fittings of the CEHs were performed with the Alloy Theoretic Automated Toolkit (ATAT) [19, 23, 24, 25] which automates most CEH construction tasks [24]. In particular the specific effective cluster interactions, *ECIs*, that make up the CEH, and their number  $n_{ECI}$ , are chosen by cross validation analysis which selects for the *most predictive* CEH; i.e. the CEH that most accurately predicts  $\Delta E_f$ s that are left out of the fit [26]. The CEH is constructed using a set of pair interactions, 3-body and 4-body interactions. Including many-body interactions is necessary to account for asymmetry in the phase diagram around equi-atomic composition. The inclusion of 4-body terms makes it possible to describe the enthalpy of mixing as a fourth-order polynomial of the composition. Experimental measurements of the enthalpy of mixing, such as through calorimetry, show that generally a fourth order polynomial is sufficient to adequately represent the experimental data [27, 28]. As many-body interactions are considered to act as corrections to the contributions from smaller clusters, generally many-body interactions rapidly decay as the number of sites increases. Therefore, the CEH is limited to 4-body ECIs. Note that the number of *ab initio* structural energies is much larger than  $n_{ECI}$ . Therefore, the system of equations for fitting the ECIs is highly overdetermined. Here, the overdeterminedness factor is defined as:

$$\chi = \frac{N_{str}}{n_{ECI}}. \quad (2)$$

$\chi < 1$  indicates a system that has no unique solution; and  $\chi = 1$  indicates a system that has a unique solution, provided it is not singular.  $\chi > 1$  implies an overdetermined systems in which unique solutions can be defined if an additional criterion is applied such as minimal sum of differences squared.

## 3. Results

### 3.1. Ground-State Analyses

Filled circles (green online) in Figs. 1a - 5a indicate values of  $\Delta E_f$  that were calculated with the VASP package, i.e.  $\Delta E_{VASP}$ . Large open squares in Figs. 1a - 5a (red online) indicate the CEH-fit to  $\Delta E_{VASP}$ . Smaller open squares ( $\Delta E_{GS}$ ; blue online) indicate the results of a ground-state (GS) analyses that included all ordered configurations with 16 or fewer anion sites, 151,023 structures. Calculated values for leave-one-out cross validation scores, (CV), and the numbers of structures,  $N_{str}$ , are indicated in the figure captions.

Additional GS analyses were performed by Monte-Carlo (MC) simulations at fixed bulk compositions, via decreasing temperature (T) scans down to T=0. The 0K  $\Delta E_f$  values from these calculations are plotted as solid-

(predicted stable) or open-diamonds (metastable; blue online) in Figs. 2a and 3a; and as small filled down-pointing triangles (blue online) in Figs. 4a and 5a. Because the calculated formation energies for the ordered configurations in Figs. 2a and 3a are negative, they constitute (falsely) predicted large-cell ordered-GS. If their formation energies are positive they can be regarded as low-energy microstructures. Note that these formation energies from MC-simulations are always upper bounds, because MC-simulations don't yield *perfectly* ordered simulation boxes.

### 3.2. Phase Diagram Calculations

First principles phase diagram calculations that were performed with the ATAT package [23, 24, 25] are plotted in Figs. 1b-5b. Additional symbols on Figs. 2b, 3b, and 4b are used to indicate various phase fields that were identified, by visual inspections of MC-snapshots: large filled down-pointing triangles (orange online) indicate disorder; up-pointing triangles (cyan online) indicate a layer structure (e.g. Fig. 2d); large checkered circles (red online) indicate a honeycomb structure (Fig. 2c); and striped circles (black and red online) indicate two-phase, assemblages, ordered plus disordered or two ordered phases.

### 3.3. Towards Phase Diagram Convergence

The procedure followed here is: 1) calculate a set of structural energies  $\{\Delta E_f\}$ ; 2) perform GS-analysis; 3) if ordered GS-phases are predicted, calculate their  $\Delta E_f$  explicitly with VASP to see if they are genuine ( $\Delta E_f < 0$ ) or false ( $\Delta E_f > 0$ ); 4) if false GS are predicted increase  $N_{str}$ . In addition to predicted GS, new structures that were added were among those that were predicted to have small  $\Delta E_f \approx 0$ . Increasing  $N_{str}$  typically generates a better approximation of the energy landscape to which the CEH is fit, and therefore yields a more realistic CEH.

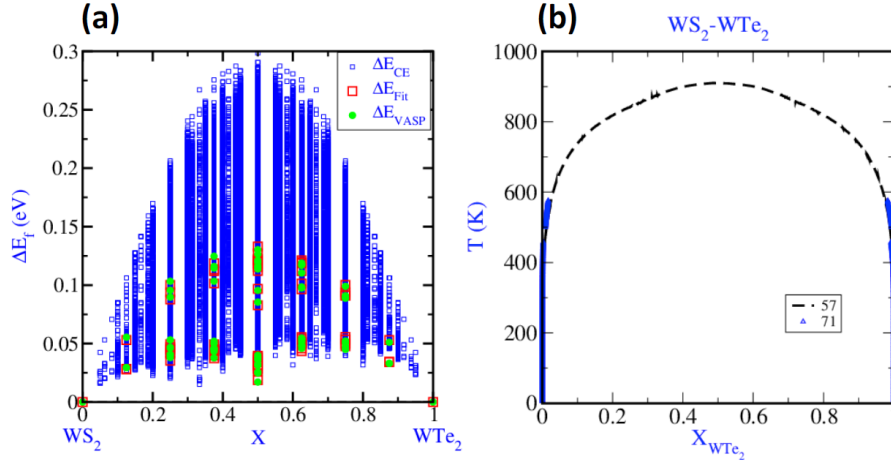


Figure 1: For  $N_{str} = 71$  with  $CV = 2.65$  meV/chalcogen atom and  $n_{ECI} = 68$ , including the point-cluster, 55 pair-, 6 3-body- and 6 4-body interactions: (a) Ground-State analysis; (b) calculated phase diagram. In (a):  $\Delta E_{VASP}$  filled circles (green online);  $\Delta E_{Fit}$  large open squares, (red online) is the CEH-fit to the DFT set;  $\Delta E_{CE}$  smaller open squares, (blue online) are the CEH-based ground-state analysis; All  $\Delta E_f > 0$  implies that there are no ordered GS, with 16 or fewer anion sites, and suggests that the phase diagram will have a miscibility gap. Note the small cross-validation score which suggests a very good CEH-fit, and in (b) the near absence of asymmetry in the miscibility gap.

## 4. Discussion

One expects that fitting CEHs to larger and larger sets of  $\Delta E_{VASP}$  ultimately leads to a converged result for the calculated phase diagram. The results presented here indicate that the fits with  $N_{str} = 71, 253, 295,$  and  $376$  (not shown) are not sufficient because: false GS are predicted, typically at  $X = 1/3$  and  $X = 1/2$ ; and qualitatively different phase diagrams are predicted with each increase in  $N_{str}$ . Standard ground-state analyses for the sets with  $N_{str} = 253, 295,$  and  $376$  (not shown) predicted no ordered GS with 16 or fewer anion sites, but MC T-scans down to  $T=0K$ , predicted false GS based on unit cells with more than 16 anion sites. The diagrams for  $N_{str} = 399$  or  $435$  are essentially identical, and may represent a converged result, however, this cannot be guaranteed at the current level of analysis.

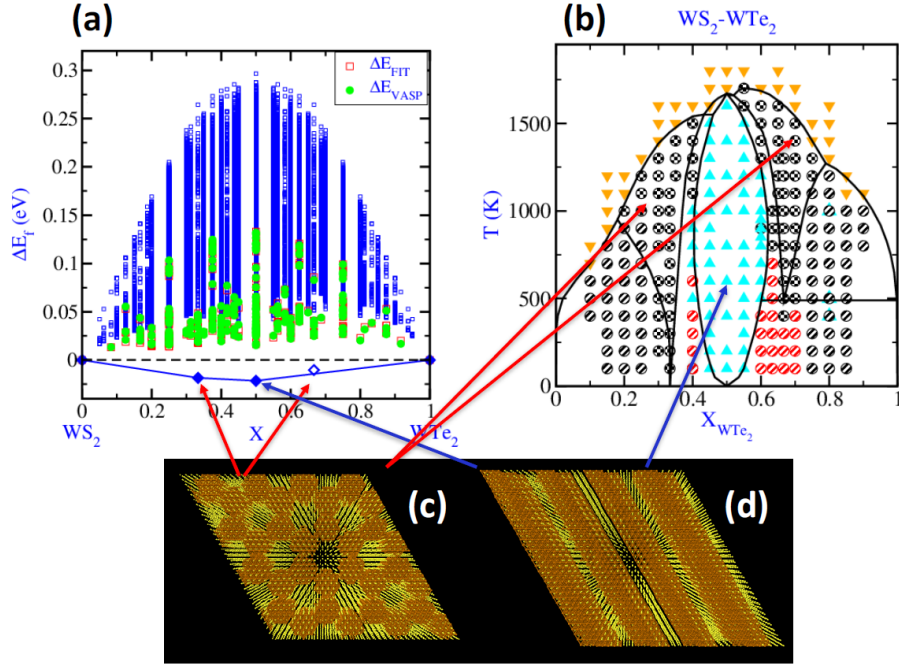


Figure 2: For  $N_{str} = 253$  with  $CV = 3.1$  meV/chalcogen atom and  $n_{ECI} = 93$ , including the so-called “empty” cluster and point-cluster, 67 pair-, 16 3-body- and 9 4-body interactions: (a) ground-state analysis; (b) calculated phase diagram. Filled diamond symbols in (a) indicate predicted GS structures as shown in the MC-snapshots of: (c) honeycomb structure at  $X = 1/3$ , and (d) a striped-phase at  $X = 1/2$ . The open diamond symbol at  $X = 2/3$  indicates a low-energy metastable honeycomb-ordered structure. Additional symbols in (b): large filled down-pointing triangles (orange online) indicate disorder; up-pointing triangles (cyan online) indicate a layer structure (d); large checkered circles (red online) indicate a honeycomb structure (c); and striped circles (black and red online) indicate two-phase, assemblages, ordered plus disordered or two ordered phases.

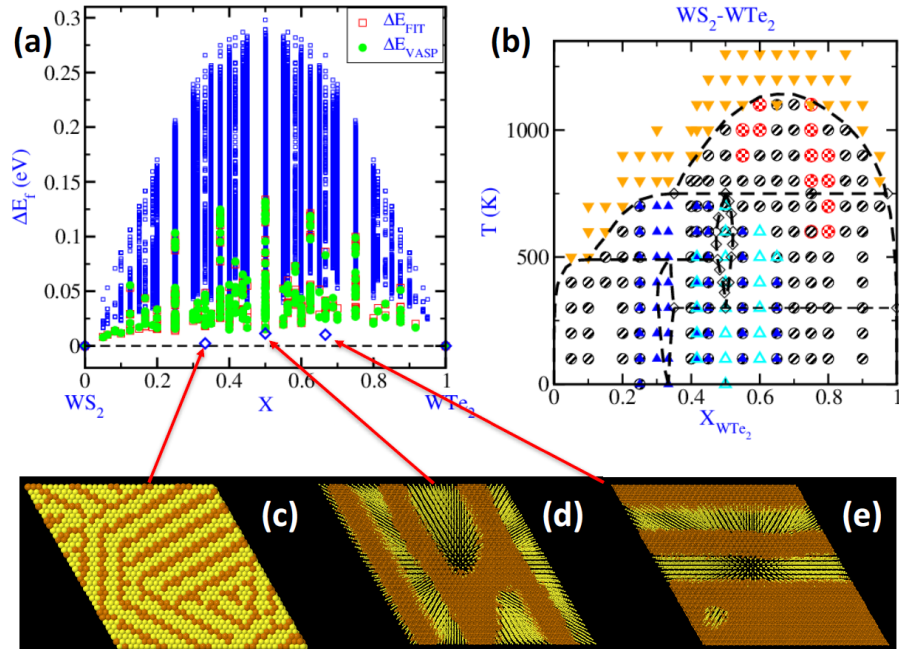


Figure 3: For  $N_{str} = 295$  with  $CV = 2.9$  meV/chalcogen atom and  $n_{ECI} = 100$ , including the so-called “empty” cluster and point-cluster, 67 pair-, 16 3-body- and 16 4-body interactions: (a) ground-state analysis; (b) calculated phase diagram. Open diamonds in (a) (blue online) indicate: (c) an ordered structure at  $X = 1/3$ ; and low-energy, mostly striped, microstructures at  $X = 1/2$  and  $X = 2/3$ . Note however, that the  $X = 1/3$ - and  $X = 1/2$ -phases appear to be stable at elevated temperatures.

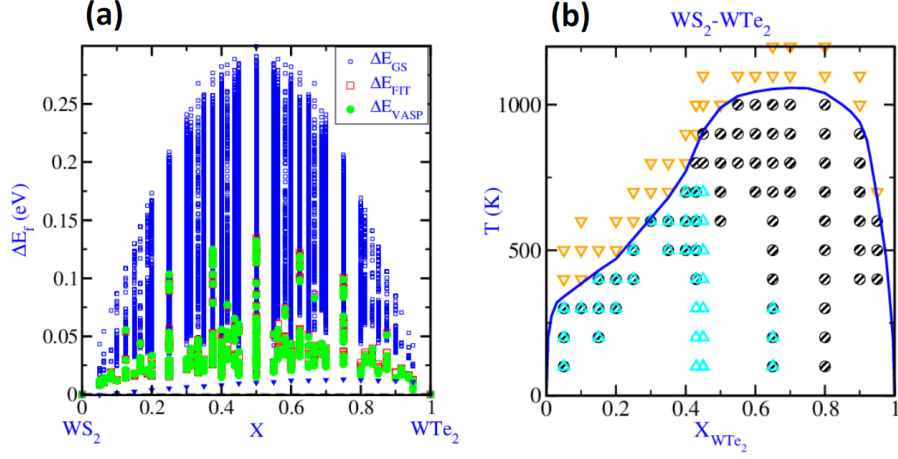


Figure 4: For  $N_{str} = 399$  with  $CV = 2.5$  meV/chalcogen atom and  $n_{ECI} = 120$ , including the so-called “empty” cluster and point-cluster, 69 pair-, 40 3-body- and 9 4-body interactions: (a) ground-state analysis; (b) calculated phase diagram. Small down-pointing triangles in (a) are  $\Delta E_{CE}$  values for MC-simulation T-scans from a low-T value to  $T=0$ . Note the asymmetry in these values. Additional symbols in (b) have the same meanings as in Fig. 2b.

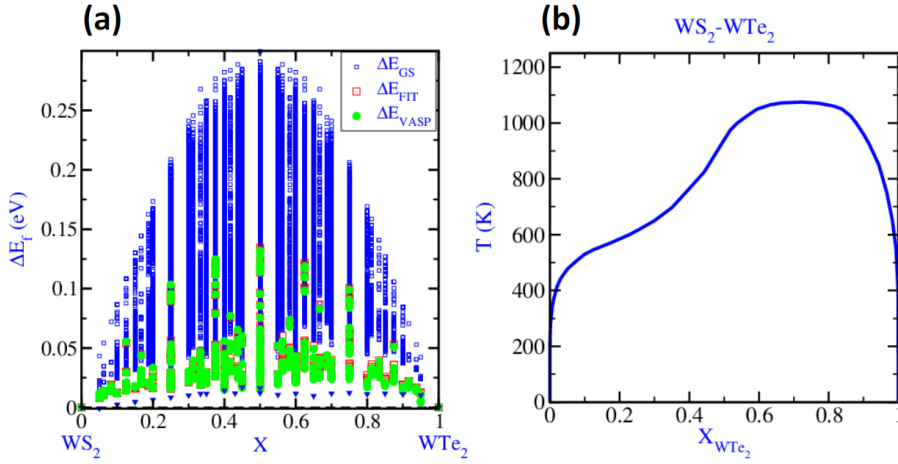


Figure 5: For  $N_{str} = 435$  with  $CV = 2.2$  meV/chalcogen atom and  $n_{ECI} = 124$ , including the so-called “empty” cluster and point-cluster, 66 pair-, 40 3-body- and 16 4-body interactions: (a) ground-state analysis; (b) calculated phase diagram. Down-pointing triangles in (a) are  $\Delta E_{CE}$  values for MC-simulation T-scans from a low-T value to  $T=0$ . Note the asymmetry in these values, which is opposite to what one expects from a size-effect argument. Compare the nearly symmetric miscibility gap in Fig. 1b with the dramatic asymmetries of Figs. 4b and 5b.

Two generalizations apply to all calculated phase diagrams for models with  $150 \lesssim N_{str} \leq 376$ : (1) When false GS are predicted, they occur in the S-rich bulk composition range  $0 \lesssim X \leq 0.5$ ; (2) The range range  $0.5 \gtrsim X \leq 1.0$  is dominated by phase separation at  $T \lesssim 1050K$ . (1) above indicates that low-energy ordered configurations on the S-rich side of the system drive the asymmetry of phase separation that is noted in (2).

Kang et al. [3] performed first-principles phase diagram calculations (with ATAT;  $N_{str} \approx 40$ ) for monolayer  $WS_2 - WTe_2$ , and reported a phase diagram with its' consolute point at  $(X, T) \approx (0.55, 680K)$ ; i.e. without the dramatic asymmetry exhibited in Figs. 4 and 5 where  $(X, T) \approx (0.7, 1075K)$ .

These results merit a closer inspection of the reliability of CEH and of the individual ECIs themselves. The large database of structural energies is an asset as it allows examination of multiple sets of clusters using multiple sets of energies. Especially when CEHs are considered with just a few ECI many sets of energies, without multiple uses of any particular energy, and thus truly independent sets of energies, are available. This allows a statistical analysis of: the average, and variation of cross validation scores; root mean square error (RMSE) of fitting; and the ECI values themselves. As overdeterminedness  $\chi$  increases, it is easy to show that RMSE and CV approach one another, with the latter always larger than the former, and in the limit of infinite  $\chi$ ,  $RMSE=CV$ . CV values are reduced when  $\chi$  is sufficiently large, and this appeals intuitively, because it removes the arbitrariness that is inherent in any particular set of structural energies that is used for fitting the CEH. At large  $\chi$  one might expect unique ECI values, as in the spirit of the method of direct configurational averaging [29]. In this sense,  $1/\chi$  is a measure of arbitrariness in the structural energy set, and thus also contributes to arbitrariness in the ECI values. Therefore, we consider the extrapolation to  $1/\chi = 0$ .

Initially, we explore a CEH in which only the 6 nearest neighbor pair ECIs are included. At least 6 formation energies are required to obtain a unique CEH. From a database of 435 formation energies, one can pick many combinations without once reusing an energy. Actually, using just 6 formation energies is not so interesting as it does not allow determination of the CV. Therefore, we use 7, or more, formation energies to determine the ECIs, the RMSE and the CV. Repeating this for each combination of energies to determine the distribution of ECI values, RMSEs, and CV values. A more or less Gaussian distribution is found with a characteristic average value, e.g.  $\overline{CV}$ , and standard deviation, e.g.  $\sigma_{CV}$ . This computation can be repeated for combinations with 8 or more formation energies, i.e. for greater  $\chi$ . Once this has been done for a sufficiently large number of  $\chi$  values the results, e.g.  $\overline{CV}$  and  $\sigma_{CV}$ , can be plotted as functions of  $1/\chi$  and extrapolated to  $1/\chi = 0$ . The details of these results are shown in a supplementary, but the main outcomes are summarized here. Larger  $\chi$  lead to larger  $\overline{RMSE}$  and to slightly smaller  $\overline{CV}$ , up to certain limiting values. The reason for increasing  $\overline{RMSE}$  is that for  $\chi = 1$  all energies can be fit exactly, but this is no longer true for larger  $\chi$ . The CEH improves as more energies are used, but soon the limitations of the small set of ECIs become apparent, and no further reduction of  $\overline{CV}$  is possible. Hence, fits at large  $\chi$  display the limitations of the particular selection of ECIs in the CEH. The standard deviations of  $\overline{RMSE}$  and  $\overline{CV}$  decrease towards zero as  $\chi$  approaches infinity, in accordance with the central limit theorem, but  $\sigma_{CV}$  does so more systematically than  $\sigma_{RMSE}$ , although the latter is generally smaller. The averaged ECI values converge towards well-defined values as  $\chi$  is increased, and their standard deviations also appear to approach small values. Note however, that the standard deviations of the ECIs are typically all of about the same magnitude for each pair ECI and each is significantly larger than  $\sigma_{RMSE}$ . For higher values of  $\chi$  they are also larger than  $\sigma_{CV}$ . This indicates that the ECIs individually do not exhibit the same convergence behavior as the RMSE and the CV.

Next, one wants to consider how an expanded CEH behaves, however, expansion greatly limits attainable  $\chi$  values, and hinders extrapolation to  $\chi = \text{inf}$ . Fortunately, it is also possible to consider a much worse CEH, e.g. by including only a single pair ECI. In that case a much higher  $\chi$  is achieved. These exercises exhibit a completely comparable trend with  $\chi$ . Single pair CEH demonstrate that when a pair with a large magnitude is chosen, the values of  $\overline{RMSE}$  and  $\overline{CV}$ , extrapolated to  $\chi = \text{inf}$ , are smaller. This confirms that CV really can be used to select the most important ECIs. A perhaps surprising result is that the  $\chi = \text{inf}$  extrapolated value of the pair ECI does not agree with the  $\chi = \text{inf}$  extrapolated value of the pair ECI obtained with the CEH with 6 pair ECIs. The single pair CEH and the 6 pair CEH converge to distinctly different ECI values for the same type of pair. The difference is larger for small-magnitude ECIs than for large-magnitude ECIs. The difference between these ECI values is larger than their standard deviations would suggest. This indicates that there are other sources of error than the sampling error due to a particular combination of structural energies that was used to fit the ECIs. In particular we expect an error due to the particular set of ECIs we selected in the CEH because ECIs that are excluded from the CEH contribute to the ECIs that are included. The smaller the number of ECIs in the CEH, and the greater the significance of the excluded ECIs, the greater this so-

called projection error will be. The  $\chi = \text{inf}$  extrapolated values of  $\overline{RMSE}$  and  $\overline{CV}$  ought to give some impression of the magnitude of the projection error that occurs in about equal measure in each and every ECI value. For this reason the small-magnitude ECIs have much larger relative errors than the large-magnitude ECIs.

Finally, there is a bias in the set of energies. Typically only near ground state structures are added as  $N_{str}$  increases. Thus  $\chi = \text{inf}$  extrapolated values of  $\overline{RMSE}$  and  $\overline{CV}$  are biased towards higher accuracy of ground state structures and lower accuracy of excited states. At elevated temperatures, non-ground state configurations contribute more to the total energy, hence the bias against them increases consolute temperatures of miscibility gaps, and temperatures of order-disorder transitions. Therefore  $\overline{RMSE}$  and  $\overline{CV}$  may give an overly optimistic impression of the accuracy of the predicted phase stability and other finite temperature properties. Clearly, the CV especially at high  $\chi$  is an important tool for constructing efficient CEHs but there are a number of weaknesses: a) it is not a measure of the accuracy of any individual ECI, but only for the whole CEH; b) it fails for individual ECIs because the CV does not account for the “projection error” of ECIs by excluded ECIs; and c) typically the CV applies to a ground state biased set of structural energies which means that finite temperature properties are less accurately represented.

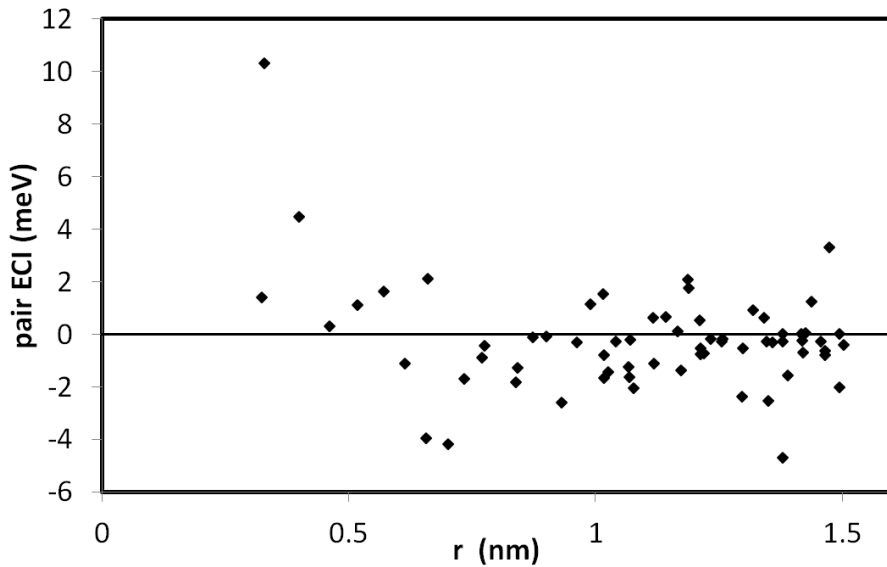


Figure 6: Effective pair interactions as function of the pair separation distance  $r$  as calculated using  $N_{str} = 435$  and  $n_{ECI} = 124$ .

In the sequence of phase diagram calculations these features can be recognized. At  $N_{str} = 71$  and  $n_{ECI} = 68$   $\chi$  is barely greater than unity giving an artificially nice fit, but without any option to check for “projection error”. Such a CEH is generally not reliable. For the other cases  $\chi \approx 3$  so that the CV and RMSE are more informative. As the individual ECIs do not have the same reliability as their collective CEH, it is not surprising that false ground states appear. To assure that the ECIs are reliable, additional tests are required: in particular the convergence towards the  $\chi = \text{inf}$  limit deserves attention, and the extrapolation should be similar for different CEH. One can also examine ECI-decay as site-separation increases. In Fig. 6 it is apparent that in final CEH with  $N_{str} = 435$  and  $n_{ECI} = 124$ , pair interactions still do not show much convergence with distance. This indicates that a system with big atomic size differences such as  $WS_2$ - $WTe_2$  requires a CEH with a very large  $N_{str}$  and  $n_{ECI}$ , or that perhaps long-ranged strain effects better be included explicitly [30].

## 5. Conclusions

A CEH-fit to at least  $N_{str} \approx 400$  is required to calculate a realistic phase diagram for the  $WS_2 - WTe_2$  TMD system; i.e. a diagram without a false GS. Low cross-validation scores do not guarantee that individual effective cluster interactions are converged to a similar degree. As errors in the individual ECIs are typically much larger than in the CEH, ground state analyses may fail even for systems with low cross validation score. In addition it is important to monitor the behavior of a CEH as a function of overdeterminedness, to rule out effects of the specific set of structural

energies that was used to derive the ECIs. Without significant overdeterminedness in the energy dataset no reliable CEH can be constructed. The typical bias towards including mostly near-ground-state structures in the energy data set favors a CEH that is ideally suited for ground states, but less so for excited states; this bias favors overestimations of transition temperatures. It is likely that the  $WS_2 - WTe_2$  system has a highly asymmetric miscibility gap as shown in Fig. 5, and that the predicted asymmetry reflects the asymmetry of lowest energy metastable ordered states, such that S-rich states consistently have lower energies than their Te-rich counterparts (down-pointing triangles, blue online, Figs. 4a and 5a).

## 6. ACKNOWLEDGEMENTS

This work was supported by NIST-MGI.

- [1] Q.H. Wang, K. Kalantar-Zadeh, A. Kis, J.N. Coleman and M.S. Strano, *Nature Nanotech.* **7**, 699 (2012).
- [2] R. Ganatra and Q. Zhang *ACS nano* **8(5)**, 4074 (2014).
- [3] J. Kang, S. Tongay, J. Li and J. Wu, *J. Appl. Phys.* **113**, 143703 (2013).
- [4] A. Kutana, E. S. Penev and B. I. Yakobson, *Nanoscale* **6**, 5820 (2014).
- [5] B. Radisavljevic, A. Radenovic, J. Brivio, V. Giacometti, and A. Kis. *Nature nanotechnology*, **6(3)**: 147, (2011).
- [6] S. Das, H.-Y. Chen, A. V. Penumatcha, and J. Appenzeller. *Nano Letters*, **13(1)**: 100, (2013).
- [7] H. Wang, L. Yu, Y.-H. Lee, Y. Shi, A. Hsu, M. L. Chin, L.-J. Li, M. Dubey, J. Kong, and T. Palacios. *Nano Letters*, **12(9)**:4674, (2012).
- [8] D. Jariwala, V. K. Sangwan, L.J. Lauhon, T. J. Marks, and M. C. Hersam. *ACS nano*, **8(2)**: 1102, (2014).
- [9] M. Fontana, T. Deppe, A. K. Boyd, M. Rinzan, A. Y. Liu, M. Paranjape, and P. Barbara. *Scientific reports*, **3**, 1634 (2013).
- [10] H. Zeng, J. Dai, W. Yao, D. Xiao, and X. Cui. *Nature nanotechnology*, **7(8)**: 490, (2012).
- [11] K. F. Mak, K. He, J. Shan, and T. F. Heinz. *Nature nanotechnology*, **7(8)**: 494, (2012).
- [12] A.K. Geim and I.V. Grigorieva, *Nature*, **499**, 419 (2013).
- [13] S.X. Wu, Z.Y. Zeng, Q.Y. He, Z.J. Wang, S.J. Wang, Y.P. Du, et al. *Small*, **8**, 2264 (2012) T.Y. Wang, H.C. Zhu, J.Q. Zhuo, Z.W. Zhu, P. Papakonstantinou, G. Lubarsky, et al. *Anal. Chem.*, **85**, 10289 (2013).
- [14] B. P. Burton and A. K. Singh *J. Appl. Phys.* **120**, 155101 (2016); <http://dx.doi.org/10.1063/1.4964868>
- [15] M.H.F. Sluiter, V. Vinograd, and Y. Kawazoe, *Phys. Rev B*, **70**, 184120 (2004).
- [16] V.L. Vinograd, B. Winkler, A. Putnis, J.D. Gale and M.H.F. Sluiter, *Chem. Geol.*, **225**, 304 (2006).
- [17] R.D. Shannon, *Acta Cryst. A*, **32**, 751 (1976). <http://abulafia.mt.ic.ac.uk/shannon/ptable.php>
- [18] G. Kresse, and J. Hafner, *Phys. Rev.* **B47**: 558 (1993); G. Kresse. Thesis, Technische Universität Wien (1993); *Phys. Rev.* **B49**: 14 251 (1994). G. Kresse, and J. Furthmüller, (1996) *Comput. Mat. Sci.* **6**: 15-50; *Phys. Rev.* **B54**: 11169 (1996); cf. <http://tph.tuwien.ac.at/~vasp/guide/vasp.html>.
- [19] Reference to specific software packages does not imply a NIST endorsement.
- [20] J. Klimes, D. R. Bowler, and A. Michaelides, *Phys. Rev.* **B83**: 195131 (2011). and *J. Phys. Condens. Matter* **22**: 022201 (2010).
- [21] <https://materialsdata.nist.gov>
- [22] J.M. Sanchez, F. Ducastelle, and D. Gratias, *Physica* **128A**, 334 (1984).
- [23] A. van de Walle, M. Asta and G. Ceder, *CALPHAD Journal* **26**, 539 (2002).
- [24] A. van de Walle and G. Ceder, *Journal of Phase Equilibria*, **23**, 348 (2002).
- [25] A. van de Walle, and M. Asta, *Modelling Simul. Mater. Sci. Eng.*, **10**, 521 (2002).
- [26] M. Sluiter, Y. Watanabe, D. Fontaine, Y. Kawazoe, *Phys. Rev. B*, **53**, 6137 (1996).
- [27] L. Kaufman, H. Bernstein, *Computer calculation of phase diagrams with special reference to refractory metals*, Academic Press, New York, isbn: 012402050 (1970).
- [28] H. Lukas, S.G. Fries, B. Sundman, *Computational Thermodynamics: The Calphad Method*, Cambridge University Press, Cambridge, isbn: 978-0521868112 (2007).
- [29] C. Wolverton, M. Asta, H. Dreyss, and D. de Fontaine, *Phys. Rev. B*, **44**, 4914 (1991).
- [30] D.B. Laks, L.G. Ferreira, S. Froyen, and A. Zunger, *Phys. Rev. B*, **46**, 12587 (1992).